Intracluster light in the core of z ~ 2 galaxy proto-clusters

Werner, S.V.; Hatch, N.A.; Matharu, J.; Gonzalez, A.H.; Bahé, Y.M.; Mei, S.; ... ; Wylezalek, D.

Monthly Notices of the ROYAL ASTRONOMICAL SOCIETY

MNRAS **523,** 91–104 (2023) https://doi.org/10.1093/mnras/stad1410
Advance Access publication 2023 May 10

Intracluster light in the core of z ∼ 2 galaxy proto-clusters

S. V. Werner [1]★ N. A. Hatch [1] J. Matharu [2,3,4] A. H. Gonzalez [5] Y. M. Bahé,[6] S. Mei,[7,8] G. Noirot[9] and D. Wylezalek [10]

[1]*School of Physics and Astronomy, University of Nottingham, Nottingham NG7 2RD, UK*
[2]*Department of Physics and Astronomy, Texas A&M University; College Station, TX, 77843-4242, USA*
[3]*George P. and Cynthia Woods Mitchell Institute for Fundamental Physics and Astronomy, Texas A&M University, College Station, TX, 77845-4242, USA*
[4]*Cosmic Dawn Center, Niels Bohr Institute, University of Copenhagen, Rådmandsgade 62, DK-2200 Copenhagen, Denmark*
[5]*Department of Astronomy, University of Florida; 211 Bryant Space Science Center, Gainesville, FL 32611, USA*
[6]*Leiden Observatory, Leiden University; Niels Bohrweg 2, NL-2333 CA, Leiden, The Netherlands*
[7]*Université de Paris, CNRS, Astroparticule et Cosmologie; F-75013 Paris, France*
[8]*Jet Propulsion Laboratory and Cahill Center for Astronomy & Astrophysics, California Institute of Technology, 4800 Oak Grove Drive, Pasadena, CA-91011, USA*
[9]*Department of Astronomy & Physics, Saint Mary's University; 923 Robie Street, Halifax NS B3H3C3, Canada*
[10]*Zentrum für Astronomie der Universität Heidelberg, Astronomisches Rechen-Institut, Mönchhofstr 12-14, D-69120 Heidelberg, Germany*

Accepted 2023 May 8. Received 2023 May 8; in original form 2022 November 9

ABSTRACT

Intracluster light is thought to originate from stars that were ripped away from their parent galaxies by gravitational tides and galaxy interactions during the build up of the cluster. The stars from such interactions will accumulate over time, so semi-analytic models suggest that the abundance of intracluster stars is negligible in young proto-clusters at $z\sim 2$ and grows to around a quarter of the stellar mass in the oldest, most mature clusters. In contrast to these theoretical expectations, we report on the detection of intracluster light within two proto-clusters at $z= 2$ using deep *HST* images. We use the colour of the intracluster light to estimate its mass-to-light ratio in annuli around the brightest cluster galaxies (BCG), up to a radius of 100 kpc. We find that 54 ± 5 per cent and 71 ± 3 per cent of the stellar mass in these regions is located more than 10 kpc away from the BCGs in the two proto-clusters. This low concentration is similar to BCGs in lower redshift clusters, and distinct from other massive proto-cluster galaxies. This suggests that intracluster stars are already present within the core 100 kpc of proto-clusters. We compare these observations to the Hydrangea hydrodynamical galaxy cluster simulations and find that intracluster stars are predicted to be a generic feature of group-sized haloes at $z= 2$. These intracluster stars will gradually move further away from the BCG as the proto-cluster assembles into a cluster.

Key words: galaxies: clusters: general – galaxies: evolution – galaxies: photometry.

1 INTRODUCTION

In the standard cosmological paradigm small density fluctuations of dark matter in the early Universe rapidly collapsed into triaxial structures called haloes, which provided a gravitational well deep enough to trap gas and produce the first stars. Over the following 13 billion years, these haloes merge to produce progressively larger haloes. What happens to the stars in these merging haloes is a matter of debate that is pivotal to our understanding of the evolution of galaxies.

Clusters of galaxies are the most massive haloes in the Universe and are therefore the most extreme examples of hierarchical merging. As such, their central galaxies, known as brightest cluster galaxies (BCGs), are uniquely suited to study the process of hierarchical galaxy formation. Early galaxy formation models (De Lucia & Blaizot 2007) predicted that BCGs would undergo protracted growth, in step with the growth of their dark matter haloes. But observations of distant BCGs conflicted with these predictions and demanded only modest growth in both size and mass since z ∼ 1 (Whiley et al. 2008; Collins et al. 2009; Chu, Durret & Márquez 2021). To account for this lack of growth, some models were updated to remove a fraction of the stars from the central galaxies of the merging haloes and deposit them as free-floating stars in the merged halo that is visible as diffuse, intracluster light (Contini et al. 2013). These new models produce modest BCG growth since z ∼ 1 and a corresponding rapid increase in intracluster light over the same period. As a result, these models predict negligible amounts of intracluster light in z ∼ 2 proto-clusters (Contini & Gu 2021). On the other hand, intracluster stars have been observed in massive clusters up to $z = 1.75$ (DeMaio et al. 2020) and $z = 1.85$ (Joo & Jee 2023), and diffuse UV light has been observed in a proto-cluster at $z = 2.2$ (Hatch et al. 2008). Therefore, intracluster light appears to be a generic feature of halo assembly, even early on, and not just a low-redshift phenomenon. Recent reviews of intracluster light observations and theory can be found in Montes (2022) and Contini (2021).

★ E-mail: stephanevazwerner@gmail.com

To test these models, we investigate the amount of intracluster light present within the core of two galaxy proto-clusters at z ∼ 2. CARLA J1018 + 053 (hereafter CARLA J1018) was discovered to be an overdensity of galaxies around a radio-loud quasar at z ∼ 1.95 (Wylezalek et al. 2013; Noirot et al. 2018), with potential intracluster light associated with the overdensity (Noirot et al. 2018). XLSSC-122 was first identified as a faint X-ray source by the XMM Large Scale Structure survey (Willis et al. 2013), which was subsequently discovered to belong to a $M_{500} = 6.3 \pm 1.5 \times 10^{13}$ $M_\odot$ halo (Mantz et al. 2018) and spectroscopically confirmed to be a large galaxy overdensity at $z = 1.98$ using *HST* grism spectra (Willis et al. 2020; Noordeh et al. 2021). Both proto-clusters contain similar amounts of stars ($\sim 10^{12}$ $M_\odot$), indicating that the two regions may contain a similar amount of dark matter. However, XLSSC-122 has a large mass gap between its first and second most massive galaxies, unlike CARLA J1018, whose three most massive galaxies have comparable masses. This suggests that XLSSC-122 has already assembled much of its dark matter into a common halo, while CARLA J1018 is still a sprawling proto-cluster consisting of several lower-mass haloes (Golden-Marx et al. 2022).

The separation between BCG and intracluster light is difficult to define observationally. Some authors use a surface brightness limit to separate between the two (e.g. Burke, Hilton & Collins 2015), whereas others fit multiple Sérsic profiles to the light and define the intracluster light to be the outermost, flat component (e.g. Zhang et al. 2019; Joo & Jee 2023). In this work, we do not try to separate the two structures due to the technical challenge of observing the faint intracluster light at high redshifts. Instead, we infer the presence of intracluster light in systems which have low concentrations of stars within the central 100 kpc of the proto-cluster. Measuring the light concentration within this radial distance is justified by the recent measurements of Joo & Jee (2023) who showed that the BCG typically dominates only the central 10 kpc region (or ∼30 kpc if the BCG is fit with two Sérsic components) for clusters above $z = 1.3$. Therefore, we will infer the presence of intracluster light in proto-clusters, which exhibit low stellar mass and light concentrations within the central 10 kpc compared to the area encompassed by a radius of 100 kpc around the BCGs, and if they contain significant light at a radial distance beyond 50 kpc from the BCG core.

Throughout this paper, we assume a flat, Λ cold dark matter cosmological model, parametrized by $\Omega_M = 0.315$, $\Omega_\Lambda = 0.685$, and $H_0 = 67.4$ km s^{-1}Mpc^{-1} (Aghanim et al. 2020), and all magnitudes are based on the AB system.

2 DATA

2.1 Protocluster sample

The protoclusters for this study were selected from a sample of four z ∼2 spectroscopically confirmed proto-clusters: XLSSC-122 at z= 1.98 (Willis et al. 2020), CARLA J1018 + 053 at $z = 1.96$, and CARLA J0800 + 4029 and CARLA J2039 − 2514 both at $z = 2.00$ (Wylezalek et al. 2014; Noirot et al. 2018). CARLA J0800 + 4029 and CARLA J2039 − 2514 were deemed unsuitable for this study due to contamination of the BCG and the surrounding intracluster light: a large foreground galaxy and bright star lies along the line of sight to the BCG of CARLA J2039 − 2514, and the most massive galaxy in CARLA J0800 + 4029 is likely to be the luminous $[F140W] = 19.7$ radio-loud quasar, SDSS J0800 + 4029.

2.2 Hubble Space Telescope Data

High resolution images for XLSSC 122 were harvested from the *HST* archive (programme ID 15267). The WFC3 images were taken through the *F*140*W* filter at four different orientations (across 12 orbits), with a total exposure time of 5171 s, and one orbit of data was taken through the *F*105*W* filter, observed at a single orientation, which resulted in a total exposure time of 2611 s. High resolution images and grism spectra were harvested for CARLA J1018 from programme ID 13740. The *F*140*W* images were taken in two orbits, each at a different orientation, for a total of 973 s. The remaining time of each orbit was used to observe through the G141 grism, details of which are provided in Noirot et al. (2016, 2018).

We performed full end-to-end processing of the *HST* images and grism data using the grism redshift & line analysis software for space-based slitless spectroscopy (Brammer 2019). The images were flat-fielded using both pixel-to-pixel flat fields and a delta correction. The sky background is fit during the cosmic ray correction step *CRCORR* by computing a linear fit to the accumulated signal from each readout. The astrometric registration uses *GAIA eDR3* data to perform a fine alignment and a final combined mosaic of all orientations for each filter was achieved using Astrodrizzle and the default distortion correction tables. The output images have a pixel scale of 0.06 arcsec. The *HST* images were masked to remove bad pixels and pixels with less than 66 per cent of the median image weight (measured from the drizzled weight images). Furthermore, the *F*105*W* image of XLSSC 122 exhibited a defect that was masked using a rectangular aperture of 10.8 by 40 arcsec, centred on [34.4286, −3.7694] and angled by 20°.

We then extracted the grism spectra from the CARLA J1018 data. A source model was constructed from the science image, which was then used to produce a contamination model for the G141 grism spectra. The contamination model was subtracted and finally the clean G141 grism spectra were extracted.

2.3 Ground-based images

Images of CARLA J1018 at broad wavebands of z, J, H, Ks, and two narrowbands at 1.06 and 1.19 μm were obtained using *FORS* and *HAWK-I* instruments on the Very Large Telescope, *ESO* via programmes 094.A-0343 and 096.A-0317. The 1.06 and 1.19 μm narrowband images were obtained because they tightly bracket the 4000 Å and Balmer breaks of galaxies at z ∼ 2, so greatly improve the photometric redshift, age, and mass measurements of the proto-cluster galaxies. The near-infrared *HAWK-I* data were reduced using standard near-infrared reduction techniques with the *ESO MVM* software (Vandame 2004). The *FORS* $z-$band data were reduced using the theli data-reduction pipeline (Schirmer 2013). We added an archival $i-$band image of this field taken on the William Herschel Telescope (Cooke et al. 2015).

Since the $z-$band image is used to measure the colour of the intracluster light, we ensured the sky background is as flat as possible through the following processes. Each exposure was first flat-fielded using dome flats. Then a single static background model was created from all the exposures taken in each night. The sources were first masked, and then exposures were median combined without any astrometric correction (to correct for the dithering) to produce a sky background model. The structure in the model included low-level fringing and gradients. Each exposure was then corrected for this background model. Finally, we eye-balled each exposure for satellite trails, anomalous reflected light, and poor chip regions and masked these regions on the individual exposures before they were coadded together to produce the final science-grade image.

Table 1. Properties of the ground-based images of CARLA J1018 used to construct the proto-cluster galaxy catalogue in Table 3. Image depths were measured in 2 arcsec diameter apertures.

Filter	3σ image depth	PSF FWHM (arcsec)
i	25.59	0.80
z	25.14	0.64
NB 1.06	23.69	0.75
NB 1.19	23.68	0.60
J	24.58	0.64
H	23.47	0.44
K	23.48	0.64

Flux and astrometric calibration for J, H, and Ks images was achieved using *2MASS* catalogues (Skrutskie et al. 2006). For the other ground-based images, relative flux calibration is done based on the universal properties of the stellar locus using stellar libraries (Pickles 1998; Ivanov et al. 2004) and applying offsets to the instrumental magnitudes so that colours of stars in the images match the reference locus. Finally, we applied Galactic extinction corrections (Schlegel, Finkbeiner & Davis 1998). Properties of these ground-based data are presented in Table 1.

The J, H, and Ks images were combined to create a deep image from which we detected sources using SExtractor (Bertin & Arnouts 1996). Since the resolution of the images varied, we Gaussian-smoothed each to match the image with the poorest resolution (the $i-$band image) before fluxes were measured within 2-arcsec-diameter circular apertures. Total fluxes were obtained by applying an aperture correction determined from the growth curves of unsaturated stars. Uncertainties on the fluxes were taken to be the square root of the photon counts in the apertures plus the standard deviation of the total photon counts within 2-arcsec-diameter apertures placed in empty regions of the images. The final object catalogue was cleaned by removing any source that was located within the regions with less than 30 per cent of the total observing time in each of the seven ground-based images.

2.4 Sky subtraction and surface brightness limits

Intracluster light has a low surface brightness and therefore is particularly sensitive to errors in the measurement and subtraction of the background light. It is therefore important to robustly measure the sky background and estimate the uncertainty in the four images we use to calculate the luminosity and colour of the intracluster light. The *HST* images will not be affected by atmospheric emission, and neither target is in a region contaminated by significant amounts of Galactic cirrus, so we expect the background light of these images to be dominated by Zodiacal light and exhibit a smooth distribution over the whole image. However, the $z-$band image comes from a ground-based instrument and is therefore subject to a variable atmospheric sky background, while the *F*105*W* can be affected by a time varying background due to 1.083 μm He I emission line from the Earth's atmosphere.

We first measure and subtract a global background from the images. To do this, we detected all sources using SExtractor. We used the default SEXTRACTOR parameters but change the following: DETECT_MINAREA = 5, DETEC_THRESH = 1.9, ANALYSIS_THRESHOLD = 1.9, DEBLEND_MINCONT = 0.005 for CARLA J1018, and further updated DETECT_THRESH = 1.7, and ANALYSIS_THRESHOLD = 1.7 to detect the fainter sources in the deeper XLSSC image. We then masked all sources to eight times their semimajor and minor axes to ensure no source light was visible. Finally, we masked the entire 150 kpc region around the BCG to ensure our background measurement was not affected by any potential intracluster light.

Table 2. Surface brightness limits. Limiting surface brightness limits for CARLA J1018 and XLSSC-122 images defined as the 3σ limit derived over a 100 arcsec^2 area.

Cluster	Filter	$\mu_{\rm lim}$(mag arcsec^{-2})
CARLA J1018	*F*140*W*	29.2
CARLA J1018	z	27.1
XLSSC-122	*F*140*W*	30.3
XLSSC-122	*F*105*W*	30.3

We fit a Gaussian to the pixel flux distribution from these masked images. The centre of the peak of the Gaussian fit is taken as the global background and subtracted from the original images. By subtracting this background pedestal, we also remove any diffuse light from unresolved faint galaxies not associated with the proto-clusters. The standard deviation of the pixel flux distribution, σ, is used to derive the limiting magnitudes through $\mu_{\rm lim} = {\rm Z_p} - 2.5 \times \log \frac{3\sigma}{\rm pix\sqrt{\Omega}}$, where $\rm Z_p$ is the zero point of the image, pix is the pixel scale, and Ω is the solid angle in arcsec^2 over which the limiting magnitude is defined. This equation only remains valid over small solid angles where the noise is dominated by pixel-to-pixel variations and Poisson noise. In order to readily compare with the depths of current and future surveys, e.g. Borlaff et al. (2022), we list the limiting 3σ surface brightness of these images in Table 2 calculated over 100 arcsec^2.

We quantify whether any large-scale variations in the background are present in the four images we use to measure the intracluster light flux and colour. To do this, we placed 5.8 arcsec-radius apertures (corresponding to 50 kpc at the redshift of the proto-clusters) in random locations over the masked images. The distribution of this background measurement conforms to a Gaussian for the *HST* images, which implies that the background noise is uncorrelated and does not contain large variations on this scale. The background in the ground-based z-band image is well matched to a Gaussian but has a tail to low fluxes. Only 6 per cent of the apertures had anomalously low fluxes. An investigation into the $z-$band image showed that these low fluxes were caused by a clustering of individual low-value pixels in a certain region of the image (far from the BCG of the proto-cluster). Thus, there is no evidence that there are large-scale variations in the background of the $z-$band image. Clustered low-valued pixels were not observed near the BCG and so this should not affect the measured colour of the intracluster light.

3 METHODOLOGY

3.1 Identifying the BCG of CARLA J1018

To identify the BCG of CARLA J1018, we first construct a galaxy member catalogue using both photometric and grism data. We used a two-step process to identify the members of the CARLA J1018 proto-cluster within the *HST* field of view. We first fitted the ground-based photometry with a suite of galaxy templates using EAZY version 0.5.2 (Brammer, van Dokkum & Coppi 2008) using no redshift prior. The templates were stepped in redshift from 0.01 to 6 over a grid of $\Delta z/(1+z) = 0.01$. During this fitting, we iteratively adjusted the zero points of the photometry to minimize the template fit residuals. We then combined the zero-point-adjusted photometric data and grism spectroscopy for the 169 sources that were detected in both data sets.

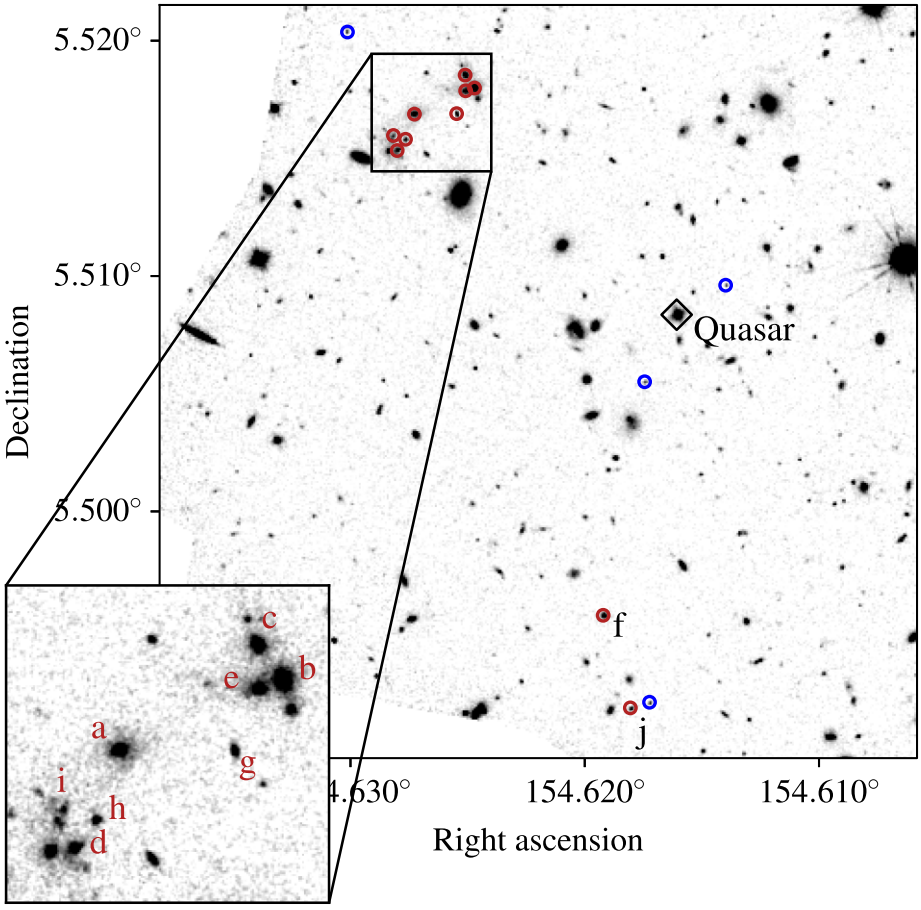

Figure 1. The *HST F*140*W* image of CARLA J1018 with marked proto-cluster galaxies. Red circles mark proto-cluster galaxies with strong continuum emission; blue circles mark emission-line galaxies that do not have enough continuum to allow us to measure their mass. The radio-loud quasar is marked by a black diamond. The insert details the region with the highest galaxy density that we take to be the proto-cluster core, with galaxy a chosen as the BCG.

We then fitted these data with a suite of galaxy templates known as Flexible Stellar Population Synthesis models (Conroy, Gunn & White 2009; Conroy & Gunn 2010) using the software GRIZLI version 1.3.2 (Brammer 2019). The templates were stepped in redshift over a coarse grid of $\Delta z = 0.004$ between the 68 per cent confidence redshift intervals determined by the EAZY fitting procedure. Finally, the templates were stepped in redshift over a fine grid of $\Delta z = 0.001$ around the peaks in the redshift probability distribution.

There are 275 sources that are detected in the *HST* image that are too faint to have counterparts in the ground-based images. These sources have low levels of continua but can be strong line emitters, so we fit their grism spectra with galaxy templates stepped in redshift from 0.01 to 6 over the same coarse and fine grids as before. We visually inspected each of the fits and removed any spectral extractions that were unreliable due to poor modelling of the contamination by nearby sources.

The best-fitting redshifts from the template fitting had uncertainties of typically $\Delta z = 0.006$ for emission line galaxies with strong continuum (e.g. galaxy *j* in Fig. 1) or with extremely strong continuum and strong Balmer/4000 Å breaks (e.g. galaxy *a*). However, for galaxies without strong emission lines, the typical uncertainty was much larger at $\Delta z = 0.05$. Therefore, selecting protocluster members by their best-fitting redshifts could introduce a bias against locating passive proto-cluster galaxies. We therefore identified proto-cluster members using two criteria.

We first selected galaxies with a best-fitting redshift within a broad window of $z_{\rm cl} \pm 0.05$, then removed those galaxies that did not have a highly peaked redshift probability distribution function over the redshift interval $z_{\rm cl} \pm 0.02$. This interval corresponds to ± 2000 km s^{-1}, which is three times the typical velocity dispersion of massive clusters at this redshift (Willis et al. 2020). We defined $I_{\rm mem}$ as the integral of the redshift probability distribution function over the redshift interval $z_{\rm cl} \pm 0.02$ and calculated this for each galaxy. We start with an initial guess of the cluster's redshift at $z_{\rm cl} = 1.95$, determined by previous work (Noirot et al. 2018), then iteratively redefine the cluster's redshift as the mean redshift of galaxies with $I_{\rm mem} > 0.5$ resulting in $z_{\rm cl} = 1.96$. $I_{\rm mem}$ is strongly dependent on the signal to noise of the data so galaxies with strong line emission or continuum have larger $I_{\rm mem}$ than lower luminosity members. We therefore eye-balled the redshift probability distribution functions and settled on the choice of $I_{\rm mem} > 0.1$ as defining the redshift probability distribution function as being 'highly peaked'. This value is low enough that it did not rule out low luminosity galaxies with Balmer/4000 Å breaks that were distinguishable by eye (such as galaxy *i*) but high enough that it removed galaxies without any clear features in the observed spectral energy distribution or the redshift probability distribution function. Using the criteria of $I_{\rm mem} > 0.1$ and having a best-fitting redshift within $z_{\rm cl} \pm 0.05$ resulting in 15 proto-cluster members, which we show in Fig. 1 and list in Table 3. The photometry and best-fitting stellar population tem-

Table 3. Properties of 15 members of CARLA J1018 identified through template fits to the combined grism spectroscopy and photometry. A map of their locations in the proto-cluster is shown in Fig. 1.

Label	Position (J2000)	Log($M_*/M_\odot$)	I_{mem}	mag	Observed M/L
Quasar	$10^h18^m27.8^s$ $+05^d30^m29.9^s$	-	1.0	19.47	-
a	$10^h18^m30.5^s$ $+05^d31^m00.6^s$	11.59	0.83	21.50	1.73
b	$10^h18^m29.9^s$ $+05^d31^m04.6^s$	11.41	0.98	21.27	0.93
c	$10^h18^m30.0^s$ $+05^d31^m06.6^s$	11.24	0.53	21.48	0.76
d	$10^h18^m30.7^s$ $+05^d30^m55.0^s$	11.08	0.95	21.49	0.53
e	$10^h18^m30.0^s$ $+05^d31^m04.1^s$	11.03	0.37	21.50	0.48
f	$10^h18^m28.6^s$ $+05^d29^m43.9^s$	11.00	0.79	22.09	0.77
g	$10h18^m30.1^s$ $+05^d31^m00.6^s$	10.77	0.40	23.27	1.34
h	$10^h18^m30.6^s$ $+05^d30^m56.6^s$	10.71	0.16	23.14	1.04
i	$10^h18^m30.7^s$ $+05^d30^m57.2^s$	10.57	0.10	22.55	0.44
j	$10^h18^m28.3^s$ $+05^d29^m29.8^s$	9.76	0.95	23.19	0.12
#162	$10^h18^m28.1^s$ $+05^d29^m30.68^s$	-	1.0	24.20	–
#446	$10^h18^m28.2^s$ $+05^d30^m19.71^s$	-	0.55	24.23	–
#354	$10^h18^m27.4^s$ $+05d30^m34.47^s$	-	0.99	24.63	–
#336	$10^h18^m31.2^s$ $+05^d31^m13.2^s$	–	1.0	24.11	–

plates for the six most massive proto-cluster members are provided in Fig. 2.

To obtain stellar masses, we fit the ground-based photometry with stellar population templates using FAST (Kriek et al. 2009). The stellar population templates are based on Bruzual & Charlot models (Bruzual & Charlot 2003) with exponentially declining star formation histories, dust attenuation, and a Chabrier initial mass function (Chabrier 2003). The redshift of the cluster members is fixed at $z_{cl} = 1.96$, but the masses do not change significantly if the redshift is fixed to the most probable grism redshift. Table 3 lists the properties of the 15 proto-cluster members, including the radio-loud quasar SDSSJ101827 + 0530 that was first used to identify this cluster. We estimate the observed $F140W$ mass to light for each galaxy using their stellar masses and observed-frame $F140W$ luminosities.

We identify six common members with the original membership catalogue from Noirot et al. (2018): the quasar, galaxy *j* (labelled *#138* in Noirot et al. 2018), and all numbered galaxies in Table 3. All numbered galaxies copy the labels given in Noirot et al. (2018). The addition of the ground-based photometry allowed us to reclassify two possible members selected by Noirot et al. (2018), their *#127* and *#647*, as being Hα emitters at a lower redshift. Galaxies labelled *a* – *i* are new detections enabled by the additional photometry and the grizli software used to reanalyse the grism data. These new detections have weaker emission lines but stronger Balmer and 4000 Å breaks than the galaxies in the original catalogue.

The selection of a BCG for the proto-cluster from Table 3 is not straightforward as the galaxies labelled *a* to *d*, as well as the quasar, could all be contenders for the most massive galaxy in the proto-cluster. To differentiate between these galaxies, we consider each galaxy's local density because the barycentre of the proto-cluster is likely to be the region with the highest galaxy density. We rule out the quasar based on its relative isolation compared to the high-density region around galaxies *a* – *d* shown within the insert of Fig. 1. Out of galaxies *a* – *d*, we select galaxy *a* as the BCG because it is the most massive and has the highest galaxy density on the scale of 100 kpc out of all galaxies in the proto-cluster.

3.2 Identifying the BCG of XLSSC-122

We use the XLSSC-122 proto-cluster membership catalogue presented in Noordeh et al. (2021) and stellar masses of the XLSSC-122 galaxies that were derived from 2-band photometry in Willis et al. (2020). However, to compare them with the stellar masses, we derive for the CARLA J1018 galaxies; we convert the stellar masses from a Salpeter Initial Mass Function (IMF) to Chabrier IMF by multiply the masses by 0.61. From this galaxy catalogue, we select the most massive galaxy as the BCG, which is galaxy *#529* at RA = 34.4342, Dec. = −3.7588, with $[F140W] = 20.64$ and a stellar mass of $5 \times 10^{11}\,M_\odot$. This galaxy lies near the centre of the X-ray contours (Willis et al. 2020) and therefore is likely to lie close to the centre of the gravitational well of the most massive dark matter halo in the proto-cluster. Due to the longer wavelength coverage of the data on the CARLA J1018 field, the masses of the CARLA J1018 galaxies are likely to be more accurate compared to those of the XLSSC 122 catalogue, which were derived from only two-band photometry ($F105W$ and $F140W$).

4 RESULTS

4.1 Quantifying the intracluster light in z∼2 proto-clusters

To isolate the diffuse light in these proto-clusters, we mask all the high surface brightness sources except for the BCG. We use the SEXTRACTOR-derived source catalogue described in Section 2.4 and mask all objects, except the BCG, to four times the semimajor and semiminor axes of objects using the SEXTRACTOR parameters (A_IMAGE and B_IMAGE). We checked the resulting masked images by eye and increased the mask size by up to 10 times the semimajor and semiminor axis, for large galaxies and very bright stars for which the smaller mask was insufficient. The masked galaxies in the 100 kpc surrounding the BCGs can be seen in Fig. 3. In this figure, we also see diffuse low surface brightness emission extending up to 100 kpc from the BCG, which resembles intracluster light.

We quantify the amount of light in the proto-cluster cores by measuring the luminosity of the BCG and intracluster light within three projected annuli of <10, 10–50, and 50–100 kpc around each BCG (marked on Fig. 3) and list them in Table 4. The inner-most aperture is likely to be dominated by light from the BCG, while the outer annulus is likely to be dominated by intracluster light (Joo & Jee 2023). The uncertainty in the background within each of these apertures was estimated by placing apertures, of the same size and shape, at random locations over the fully masked image described in the section above on sky subtraction and image depth. The standard deviation of the fluxes (within the ∼1000 apertures that have a comparable unmasked area as the regions of interest) is taken as the uncertainty in the sky background.

We find that both proto-clusters contain at least two times more light in the region beyond 10 kpc than within 10 kpc of their central galaxies, demonstrating that these proto-clusters host significant

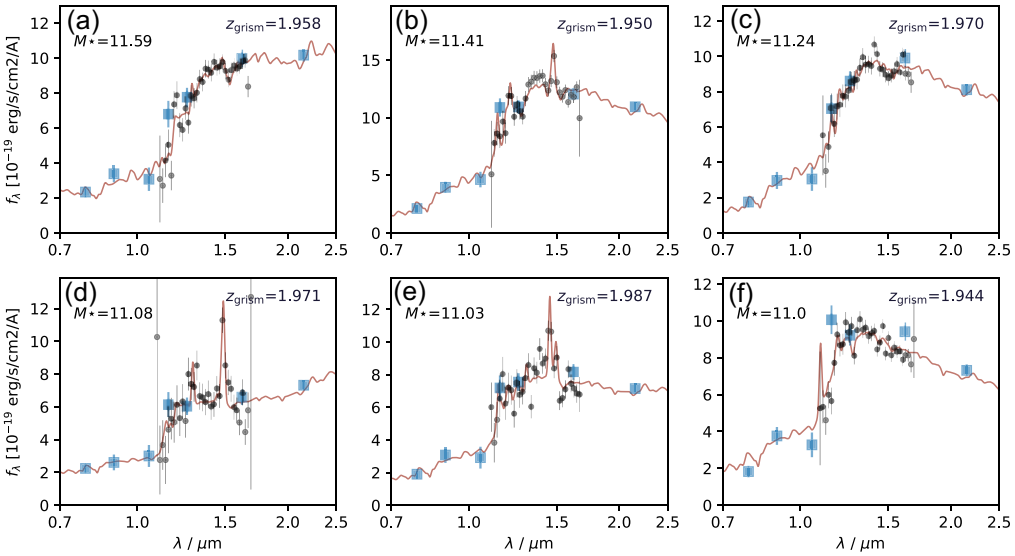

Figure 2. Spectral energy distributions of the six most massive galaxies in CARLA J1018. The black circles show the grism spectral data, while the blue squares show the photometry from the ground-based images. The galaxy template that best fits the spectral energy distribution is shown in red.

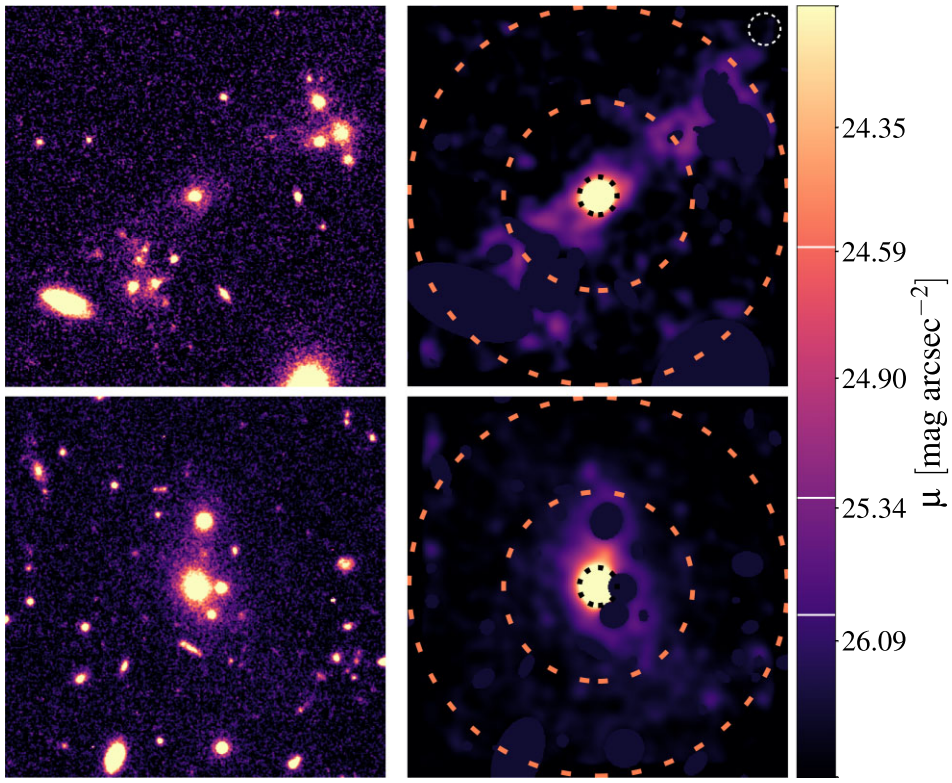

Figure 3. *HST* images of the core of the CARLA J1018 + 0530 (upper panels) and XLSSC 122 (lower panels) proto-clusters (F140W band). The left images show the BCG, intracluster light, and surrounding galaxies at the native resolution of the *HST* images. On the right, we highlight the light from the intracluster stars by masking all galaxies, except for the BCG, then smoothing the remaining pixels with a Gaussian 2D kernel of $\sigma = 0.12$ arcsec. The dashed circles mark a radial distance from the BCG centre of 10, 50, and 100 kpc. The white lines on the colour bar marks the 3σ (7σ), 5σ (12σ), and 10σ (24σ) depths in the CARLA J1018 + 0530 (XLSSC 122) images within an area of 1 square arcsec, as shown by the white circle in the top right.

amounts of intracluster light. We also measure the total light within a 100 kpc-radius circular aperture and defined the concentration of light as the luminosity within 10 kpc compared to the luminosity within a 100 kpc radius, with uncertainties resulting from the fractional errors in the 10 and 100 kpc apertures added in quadrature. We find the light concentration in the centre of the XLSSC 122 proto-cluster is 0.29 ± 0.03 and 0.23 ± 0.02 in the CARLA J1018 proto-cluster.

We check whether the presence of diffuse light is unique to the BCGs or is a generic feature of massive proto-cluster galaxies by comparing the projected circular radial profiles of the BCGs to other proto-cluster galaxies with similar stellar masses of more than

Table 4. The *F*140*W* surface brightness, *F*140*W* luminosity, and stellar mass of the BCG & intracluster light within the z ∼ 2 proto-clusters. The luminosity was measured inside circular apertures and annuli centred on the BCG. The uncertainties account for any residual variations in the background as they are measured from the standard deviation of flux measured in ∼1000 randomly distributed apertures across each image. Note that the stellar mass uncertainties are purely statistical and do not account for systematic uncertainties due to the uncertain mass-to-light ratio (see Section 5.4 for details). The average surface brightness within each aperture is greater than the 3σ surface brightness limit of the images that is listed in Table 2.

	Surface brightness (mag arcsec^{-2})			Luminosity (10^{11} L$_\odot$)			Stellar mass (10^{11}M$_\odot$)		
Aperture (kpc)	<10	10–50	50–100	<10	10–50	50–100	<10	10–50	50–100
CARLA J1018	23.37 ± 0.02	26.4 ± 0.1	27.2 ± 0.1	1.8 ± 0.1	2.4 ± 0.2	3.2 ± 0.4	1.5 ± 0.1	0.8 ± 0.1	1.0 ± 0.1
XLSSC 122	22.77 ± 0.01	26.1 ± 0.1	27.5 ± 0.1	2.2 ± 0.1	2.6 ± 0.1	2.8 ± 0.4	1.2 ± 0.1	1.4 ± 0.1	1.6 ± 0.2

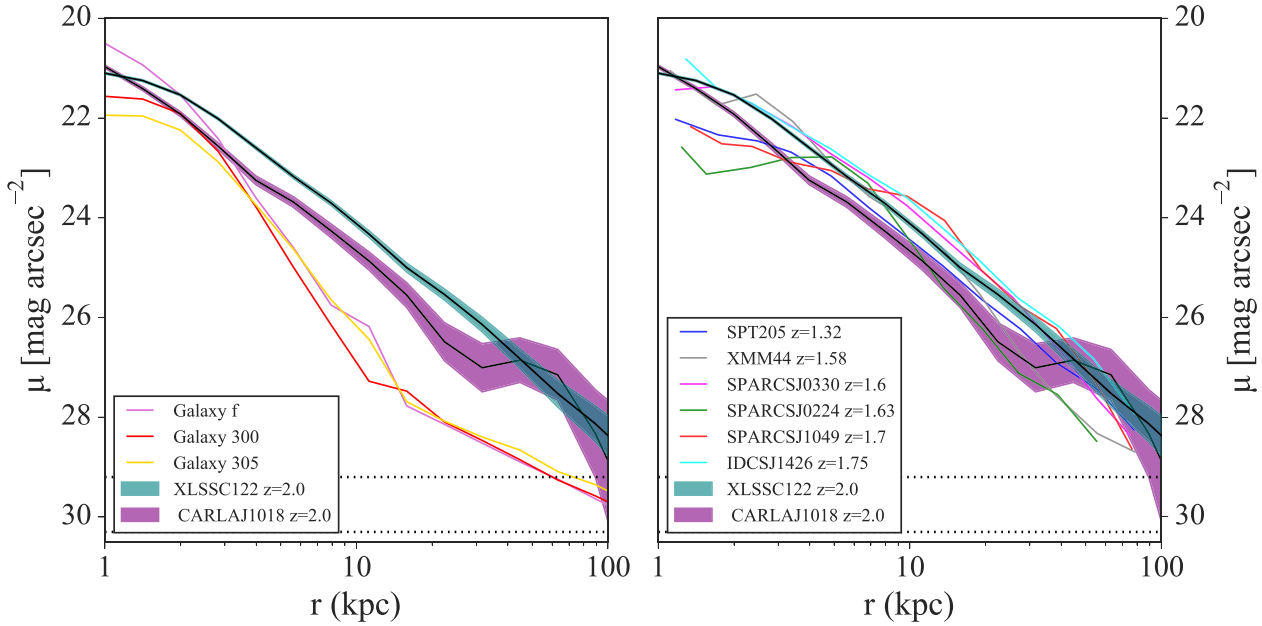

Figure 4. Radial surface brightness profiles for the BCG within the CARLA J1018 (purple) and XLSSC 122 (blue) proto-clusters. All other galaxies were masked from the *F*140*W HST* images. The horizontal dotted lines at the bottom of the figures show the 3σ image depths for CARLA J1018 (top) and XLSSC 122(bottom). In the left-hand panel, we compare the surface brightness profiles of the BCGs to the three most massive galaxies within the proto-clusters that lie far outside the cores (*# 300* and *# 305* from XLSSC 122, Noordeh et al. 2021, and galaxy *f* within CARLA J1018). The BCGs have a uniquely extended morphology that is not shared by other proto-cluster galaxies. In the right-hand panel, the surface brightness profiles are compared to BCGs at lower redshifts (DeMaio et al. 2020); redshift-corrected to $z = 2$ to enable a direct comparison with the two proto-clusters at z∼2.

10^{11} M$_\odot$. We only find three galaxies with such high masses outside the central 100 kpc of the proto-clusters [galaxies labelled *#300* and *#305* in XLSSC 122 by Noordeh et al. (2021) and galaxy *f* from CARLA J1018]. The surface brightness profiles of these three galaxies, shown in the left-hand panel of Fig. 4, are much steeper than the BCGs, and the light concentration of these galaxies are all greater than 0.89, which is three times higher than either of the BCGs. The BCGs therefore have a distinct light profile that is more extended than other massive proto-cluster galaxies.

In the right-hand panel of Fig. 4, we compare the light profile of the z ∼ 2 BCGs to BCGs at $z \sim 1.5$ that are known to be surrounded by intracluster light (DeMaio et al. 2019). Joo & Jee (2023) performed multi-Sérsic fitting to many of these profiles and found that light in the inner 10 kpc was dominated by the BCG, whereas light beyond 10 kpc was either dominated by the intracluster light component, or dominated by an extended, flat-bulge component of the BCG up to at most 30 kpc, and then intracluster light dominated beyond. The surface brightness profiles of the proto-cluster BCGs have remarkably similar profiles to the $z\sim$ 1.5 cluster BCGs beyond 10 kpc, which we interpret as evidence that intracluster light is already present in these proto-clusters.

4.2 Stellar mass and concentration of the BCG and intracluster stars

To compare our discovery of intracluster light within proto-clusters to the predictions of simulations, such as Contini & Gu (2021), we need to convert the luminosity to an estimate of the stellar mass. We use the colour of the light to estimate the mass-to-light ratio in each annulus. We combine the *HST F*140*W* images with images of light from below the Balmer break in the rest frame of the proto-cluster galaxies. For XLSSC 122, we use an *HST* image taken through the *F*105*W* filter, while for CARLAJ1018, we use a $z-$band image taken from the ground (from VLT). We estimate the colour of the light in three radial bins for XLSSC 122 and two wider bins for the shallower CARLA J1018 images and compare them to the colours of the proto-cluster galaxies in Fig. 5.

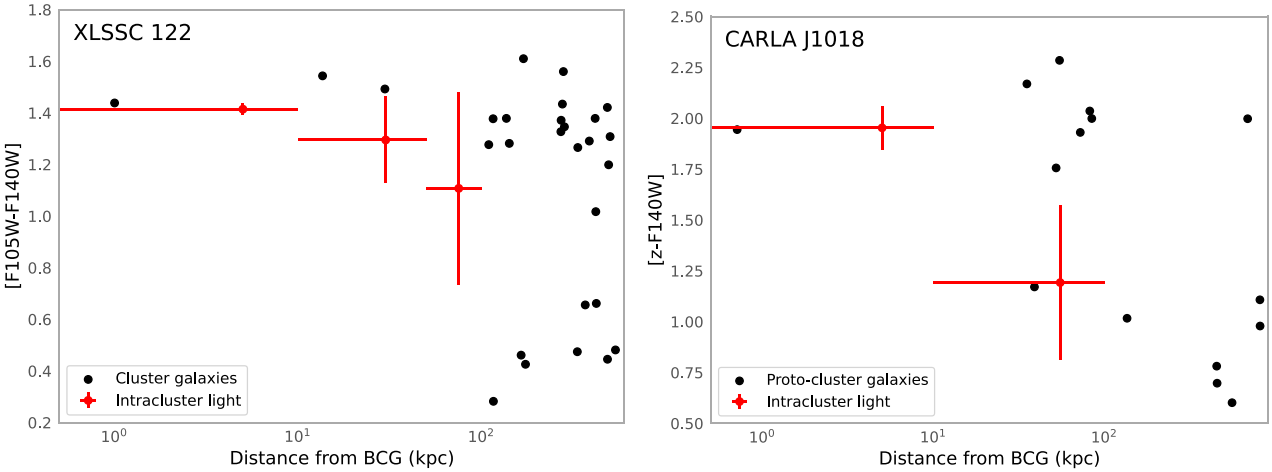

Figure 5. The colour of the BCG and intracluster light (red) compared to the proto-cluster galaxies (black dots) in XLSSC 122 (left) and CARLA J1018 (right). The intracluster light in XLSSC 122 has a similar colour to the red proto-cluster galaxies, and we assume that the intracluster stars have the mass-weighted mass-to-light ratio of protocluster galaxies with colours of $[F105W - F140W] > 1.1$. The colour of the intracluster light in CARLA J1018 is significantly bluer in the outskirts than in the core region. We therefore calculate the mass of the stars within 10 kpc using the mass-weighted mass-to-light ratio of protocluster galaxies with colours of $[z - F140W] > 1.5$, while the mass of the stars beyond 10 kpc are calculated using the mass-weighted mass-to-light ratio of protocluster galaxies with colours of $[z - F140W] < 1.3$.

The light within 100 kpc of the BCG of XLSSC 122 has a similar $[F105W] - [F140W]$ colour as the proto-cluster members that reside on the red sequence ($[F105W] - [F140W] > 1.1$). We assume that the intracluster light is produced by the stripping and destruction of proto-cluster galaxies, and that all galaxies are stripped equally. Under these assumptions, it is appropriate to use the mass-weighted mass-to-light ratio of all the XLSSC-122 proto-cluster galaxies with $[F105W] - [F140W] > 1.1$. Using the stellar masses (renormalized to a Chabrier IMF) listed by Noordeh et al. (2021), we find that such red galaxies contain a total mass of 10^{12} $M_\odot$. We transform the observed fluxes into absolute magnitudes to derive a total $F140W$ luminosity of 1.8×10^{12} $L_\odot$. Thus, the observed mass-to-light ratio through the $F140W$ filter is 0.56 for the light in XLSSC 122.

The colour of the light within the core of CARLA J1018 varies with radius. To compare the colour of the diffuse light with the colour of the galaxies, we perform aperture photometry on the $F140W$ and $z-$band images using four times the semimajor and semiminor axis of the catalogues detected by SExtractor for the masking. These large apertures are chosen to ensure we have all the galaxies' light, even in the ground-based $z-$band image, which has a larger PSF than the space-based $F140W$ image.

In the inner 10 kpc, the light matches the colour of the red sequence galaxies with $[z - F140W] > 1.7$. The mass-weighted mass-to-light ratio for these galaxies is 0.89, which we adopt for the light within this aperture. This ratio is larger than that found for XLSSC 122 because XLSSC 122 contains several bright, low-mass galaxies that bring down the mass-averaged mass-to-light ratio of the red galaxies. The CARLA J1018 $F140W$ and grism data are shallower than the XLSSC 122 data, which results in fewer detections of low-mass red galaxies. However, any undetected low-mass galaxies are unlikely to greatly influence the mass-averaged mass-to-light ratios: the core region of CARLA J1018 contains several 10^{11} $M_\odot$ galaxies, which negate the impact of any (undetected) low-mass galaxies on the mass-averaged mass-to-light ratios.

Beyond 10 kpc, the diffuse light of CARLA J1018 is significantly bluer and is similar to galaxies *i* and *j*. The other five blue galaxies do not have measurable masses as they are not detected in the images taken by the VLT, and therefore they cannot be included in this calculation. The mass-weighted mass-to-light ratio of galaxies *i* and *j* is 0.32.

We convert the light measured in each aperture to stellar mass using these mass-to-light ratios and list them in Table 4. The main limitation of these results is the strong dependence of the stellar concentration on the assumed mass-to-light ratios for each radial bin. Simulations suggest that the intracluster light comes from stripping of the massive galaxies in the forming cluster (Merritt 1984; Rudick, Mihos & McBride 2006), which justifies our using the mass-weighted mass-to-light ratios of the galaxies to estimate the mass-to-light ratio of the intracluster stars. However, to be cautious, we explore how alternative mass-to-light ratios affect our conclusions in Section 5.4. We define the concentration of stellar mass as the fraction of stellar mass within 100 kpc that lies within the central 10 kpc, $\frac{M_*(<10kpc)}{M_*(<100kpc)}$, and find that the stellar mass is more centrally concentrated in CARLA J1018, with $\frac{M_*(<10kpc)}{M_*(<100kpc)} = 0.46 \pm 0.05$, compared to XLSSC 122, with $\frac{M_*(<10kpc)}{M_*(<100kpc)} = 0.29 \pm 0.03$. The quoted uncertainties are only from uncertainties in the light measurement within each aperture and do not include any systematic uncertainty from the assumed mass-to-light ratio. In Fig. 6, we compare these stellar mass concentrations of the proto-cluster cores with lower redshift clusters from the sample of DeMaio et al. (2020).

The stellar mass concentration of the lower redshift clusters exhibits a mild trend with halo mass and no dependency on redshift. XLSSC 122 lies on the same relation of concentration-halo mass as the lower redshift clusters, and we use this relation to estimate a halo mass of CARLA J1018 based on its stellar mass concentration. To find a relation between $\frac{M_*(<10kpc)}{M_*(<100kpc)}$ and $M_{500,c}$, where $M_{500,c}$ is the mass within the radius at which the density is 500 times the critical density of the Universe, we applied a least-squares algorithm to all clusters in the sample of DeMaio et al.

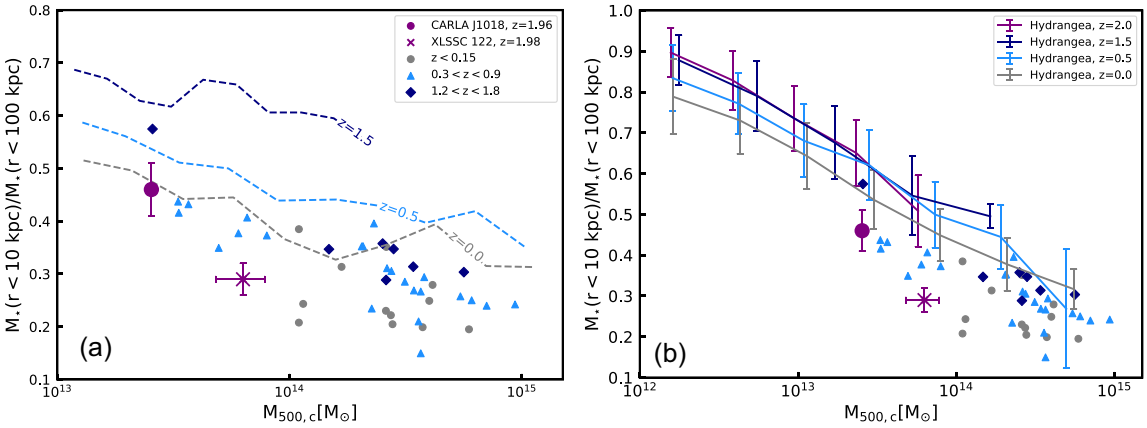

Figure 6. The concentration of stellar mass within the z ∼ 2 proto-clusters (purple symbols), defined as the ratio of stellar mass within 10 kpc to the stellar mass within 100 kpc, versus the total halo mass ($M_{500,c}$). Grey and blue symbols show lower redshift clusters gathered from the literature (DeMaio et al. 2020), which suggests an inverse relationship between the stellar mass concentration of the core and the total cluster mass ($M_{500,c}$). In the left-hand panel, the dashed lines display the predicted concentrations from the semi-analytic models of Contini & Gu (2021), while in the right-hand panel, the solid lines display the predicted concentrations from the Hydrangea hydrodynamical simulations (Bahé et al. 2017).

(2020), regardless of their redshift. We derive the following relation: $\frac{M_*(<10kpc)}{M_*(<100kpc)} = 2.57 - 0.16 \times \log M_{500,c}$. The stellar concentration of 0.46 within CARLA J1018 implies an approximate total cluster mass of $M_{500,c} \sim 10^{13.4} M_\odot$. We note this is within a factor of five of the halo mass estimate of Mei et al. (2022) based on the galaxy overdensity, but both estimates should be considered unreliable as they have been derived through methods that have not been well tested.

4.3 Comparing the proto-cluster stellar mass concentration to simulations

The concentration of stellar mass in the central 100 kpc of these proto-clusters provide us with a well-defined quantity that we compare to two state-of-the-art simulations of intracluster light formation. In Fig. 6a, we compare our data to the predictions of intracluster light from the semi-analytic model of Contini & Gu (2021). The intracluster stars in this model are produced from an analytic model that takes a fraction of the stars from satellite galaxies as they orbit the BCG, as well as harvesting a fraction of the stars from galaxies merging with the BCG. Full details of the model are provided in Contini et al. (2013).

Once stripped, the intracluster stars are assumed to follow an NFW profile (Navarro, Frenk & White 1997) adapted such that the concentration parameter of the intracluster light, C_{ICL}, is modulated by a constant, $\gamma(z)$. By varying the stellar concentration parameter, these simulations can reproduce the observed stellar mass within 100 kpc of the centre of clusters at $0 < z < 1.5$ (Contini & Gu 2020). We use the optimal concentrations derived by Contini & Gu (2020): $\gamma(0) = 3$, and $\gamma(> 0) = 5$, for the lines shown in Fig. 6a.

These models are designed to match the observed slow growth rate of the BCG; so, in this simulation, the BCG is mostly assembled by $z \sim 1$ and the surrounding intracluster light builds up around it over the following 7 Gyr. The stellar concentrations therefore decrease with decreasing redshift as stars from mergers and stripping preferentially accumulate beyond the outskirts of the BCG. The highest redshift model predictions are at z ∼ 1.5, since above this redshift the intracluster light is predicted to be negligible and the stellar concentrations tend towards unity.

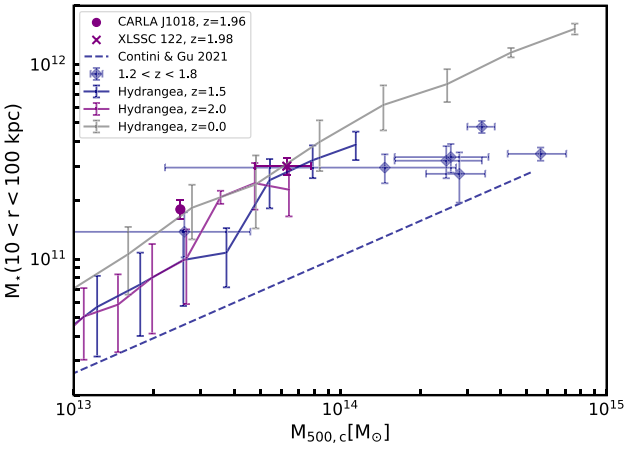

Figure 7. The amount of stellar mass in the annulus $10 < R < 100$ kpc around the BCGs in the $z = 2$ proto-clusters (purple symbols), and $z \sim 1.5$ clusters from (DeMaio et al. 2020, blue diamonds), versus the total halo mass, $M_{500,c}$. The dashed blue line displays the predicted concentrations from the semi-analytic models of Contini & Gu (2021) at $z = 1.5$, and the solid lines display the predicted concentrations from the Hydrangea hydrodynamical simulations (Bahé et al. 2017) at three different redshifts. The Hydrangea simulations are in reasonable agreement with the observations in the overlapping mass range ($M_{500,c} < 10^{14} M_\odot$), whereas the semi-analytic models underpredict the amount of intracluster stars at these high redshifts.

The Contini & Gu (2021) predictions agree reasonably well with the observed concentrations at $z = 0$ and 0.5, although the predictions are higher than most of the observations. The main discrepancy occurs at $z = 1.5$ where the models have significantly higher concentrations than both $z \sim 2$ proto-clusters as well as other clusters at $z \sim 1.5$. This remains true regardless of the assumed halo mass of CARLA J1018. As shown fig. 1 of Contini & Gu (2021), and reproduced in Fig. 7, these models underpredict the mass of intracluster stars at $z = 1.5$ within the $10 < R < 100$ kpc annulus surrounding the BCGs, which explains why the predicted concentrations are much higher than observed. Our discovery of

BCGs at $z \sim 2$ with low stellar concentrations and significant stellar mass at >10 kpc implies that the formation of the intracluster light began earlier than predicted by this model.

We next compare the observed stellar mass concentrations to the Hydrangea hydrodynamical simulations (Bahé et al. 2017). These are a suite of 24 zoom-in simulations of massive galaxy clusters within which the equations of gravity are solved for collisionless dark matter and stellar particles, with additional hydrodynamical equations solved for gas particles. Numerical subgrid algorithms are used to solve for the other ingredients of galaxy formation, such as cooling, star formation, stellar feedback, and black hole growth (see see Schaye et al. 2015 and Bahé et al. 2017 for details).

The positions of star particles are traced throughout the simulation so the stellar distribution can be used to test the fidelity of the model. Using these simulations, Alonso Asensio et al. (2020) showed that the distribution of the intracluster stars closely follows that of the total mass distribution at $z \sim 0$. This agrees with recent observations that showed the intracluster light followed the mass distribution within the central 140 kpc (Montes & Trujillo 2018). However, we caution that these simulations produce too many stars in the centre of clusters, and the BCGs end up three times too massive by the present day (Bahé et al. 2017). This means that the galaxy model has not yet solved the issue of restraining the BCG stellar growth.

To create the data shown in Fig. 6b, we extracted the stellar mass concentration within four snapshots of the simulations: $z = 0.0$, $z = 0.47$, $z = 1.49$, and $z = 1.99$. Within each snapshot, we identified the central galaxy (the BCG) of each dark matter halo with a mass greater than 10^{12} $M_{\odot}$. The stellar mass concentration is calculated as the ratio of stellar mass within a projected radius of 10 kpc to the stellar mass within a projected radius of 100 kpc, excluding any stars within these 2D apertures that are gravitationally bound to satellite galaxies. We separated the data from each snapshot into halo mass bins, then calculated the median stellar mass concentration and the standard deviation of the concentration for the haloes in each halo mass bin, which are displayed in Fig. 6b.

In these hydrodynamical simulations, the redistribution of stars during mergers and stripping depends only on gravity and the position of stars within galaxies. Hence, the distribution of BCG and intracluster stars in this simulation is a direct prediction of hierarchical merging, modulated only by the galaxy evolution model.

We find that the concentrations from these simulations are in reasonable agreement with the observations at z = 0 and 0.5, although the simulations tend to have higher concentrations than the observations, similar to the semi-analytic models mentioned above.

In contrast to the semi-analytic models of Contini & Gu (2021), the concentrations of the hydrodynamical simulations at $z > 0.5$ have little further evolution with redshift in the $M > 10^{13}$ $M_{\odot}$ mass regime, and only minor evolution at lower masses. In general, the hydrodynamical simulations predict that the stellar concentration depends on the halo's total mass but has relatively little dependency on redshift, especially at $z > 0.5$. Thus, there is no redshift at which the model does significantly worse at reproducing the observations; the stellar light is slightly more concentrated in the simulated haloes than in the observations at all redshifts probed.

Bahé et al. (2017) has, however, shown that the simulations produce BCGs that are too massive, which can impact the stellar concentrations. Therefore, we also compare the predicted and observed stellar mass in the annulus $10 < R < 100$ kpc surrounding the BCGs in Fig. 7. The Hydrangea simulations predict a similar amount of intracluster stars to the observations at $M_{500,c} < 10^{14}$ $M_{\odot}$, but unfortunately do not probe haloes of masses $M_{500,c} > 10^{14}$ $M_{\odot}$ where most of the $z \sim 1.5$ observations exist. The stellar mass within this region of the two proto-clusters lies on the upper bound of the predictions, but within the scatter.

The Hydrangea simulations, therefore, predict a level of intracluster light that is consistent with the observations at $z = 2$, but the concentrations are higher than observed because the simulations produce too much mass in the central 10 kpc of the BCG. We therefore still lack a simulation model that can predict realistic amounts of intracluster light at $z = 2$ while also restraining excessive BCG growth.

5 DISCUSSION

5.1 The implications of finding intracluster light in proto-clusters

Our work extends the baseline over which intracluster light has been investigated to $z \sim 2$. At this epoch, typically less than 20 per cent of the matter that will end up in the cluster has assembled into the main halo (Muldrew, Hatch & Cooke 2015), and the haloes that we have observed are below the general limit of a cluster-sized halo and more akin to galaxy groups. But our images show that the central 100 kpc of these proto-clusters already contain intracluster stars.

The Hydrangea simulations agree that intracluster light can exist at such a high redshift and go further to suggest that intra-halo stars, i.e. stars that are in haloes but gravitationally unbound from any galaxy, are present in massive haloes up to at least $z \sim 2$. As these massive haloes merge to form larger groups and accrete onto clusters their intra-halo stars will combine. Stars that were already unbound from galaxies when they accrete onto the cluster are defined as having been 'pre-processed'. Since the Hydrangea simulations suggest that all massive haloes contain intra-halo stars, it is likely that pre-processed stars are a significant source of intracluster stars. Therefore, semi-analytic simulations should take care to include intra-halo stars at $z > 1$, even in haloes of masses as low as 10^{12} $M_{\odot}$.

Our findings also argue against a significant contribution of intracluster stars within the central 100 kpc coming from the stripping of satellite galaxies as they orbit in the cluster. Such a stripping mechanism would build up intracluster light over time, regardless of whether the halo grows significantly in mass. Thus, if stripping of orbiting satellites were a dominant contributor to intracluster stars, we would expect the stellar mass concentration to strongly depend on redshift and only weakly depend on halo mass. Such evolution in the stellar mass concentration can be seen in the models of Contini & Gu (2021) displayed in Fig. 6a, but these do not match the trends seen when combining our data with the larger sample from DeMaio et al. (2020).

Our observational data find the opposite trends: a dependence on halo mass and little (or no) dependence on redshift. The stellar mass concentration in the $z \sim 2$ proto-clusters is comparable to group-sized haloes at $0.1 < z < 0.9$, which have similar masses. The groups at $z < 0.9$ have had much more time to strip stars from satellites than the $z \sim 2$ proto-clusters, thus such stars cannot be a major source of intracluster stars within the central 100 kpc. It is plausible, however, that such stars contribute much more to the intracluster light at larger radii.

These results support the recent finding of Ko & Jee (2018) and Joo & Jee (2023), which revealed massive clusters at $z \sim 1$ that contained ~17 per cent of the total stellar light of the clusters within the diffuse intracluster component, which is similar to the fraction of intracluster light (ICL) in local clusters. These authors suggested that the dominant form of intracluster light production

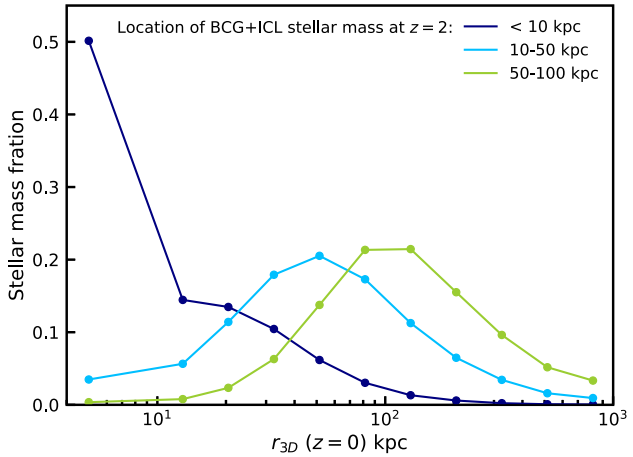

Figure 8. The location where the stellar mass of the Hydrangea proto-clusters' BCG and intracluster light ends up by $z = 0$. The coloured lines show the $z = 0$ location of stars that were located at $z = 2$: within 10 kpc of the BCG centre (dark blue); between 10 and 50 kpc (light blue); and between 50 and 100 kpc (green).

could be through the accretion of pre-processed stray stars, and our observations provide evidence of an abundance of such stars in proto-clusters.

5.2 The fate of the BCG and intracluster stars found in proto-clusters

The amount of intracluster stars in the proto-clusters is likely to increase over time because the proto-clusters are likely to evolve into clusters that are an order of magnitude more massive (Muldrew et al. 2015). As we can see from Fig. 7, such massive clusters are predicted to have significantly more stellar mass in the $10 < R < 100$ kpc region than their low mass progenitors. Furthermore, local clusters are known to have significant intracluster light at more than 100 kpc distant from the BCG.

In Fig. 8, we explore the fate of the stars within 100 kpc of the $z = 2$ BCGs that were identified in the $M > 10^{13}\,M_{\odot}$ Hydrangea haloes. We first divide the stellar population at $z = 2$ into three radial bins: <10 kpc, between 10 and 50 kpc, and between 50 and 100 kpc. We then plot the fraction of stellar mass within each of these bins that ends up at various radii within the cluster at $z = 0$. Since we want to know where the $z = 2$ stars end up, the stellar mass of each stellar particle is always taken as the one measured at $z = 2$. By $z = 0$, however, stellar mass loss will reduce the mass of the stellar particles, but this does not change the profiles significantly.

Over time, the $z = 2$ stars diffuse from their initial position with most stars moving to larger radii. Only half of the stars that lay within the central 10 kpc of the BCG remain within the same region. The other half move further out and a few per cent reach distances of more than 100 kpc. Similarly, approximately half of the stars in the $10 < R < 50$ kpc bin remain in the same location and the other half move to larger distances; almost a quarter of the stars travel to distances larger than 100 kpc. The largest amount of movement occurs in the $50 < R < 100$ kpc bin, where only ∼30 per cent of the stars remain in the same bin by $z = 0$ and over 55 per cent move further out beyond 100 kpc and several per cent reaching distances of over 400 kpc. Overall, by $z = 0$, the stars end up further away from the BCG than at $z = 2$.

Spread over such a large area, the resulting surface brightness from the stars at $R > 100$ kpc would likely be below current measurements of nearby clusters. Therefore, further production of intracluster stars or accumulation of previously stripped stars from infalling groups (e.g. Bahé et al. 2019) must occur to result in the prominent intracluster light seen at several 100 kpc from the BCGs in present-day massive clusters. Such growth in the intracluster light is expected given the results of Burke et al. (2012) and DeMaio et al. (2020), who showed that the stellar mass in clusters grows from the inside-out. Burke et al. (2012) showed that the low-surface brightness light ($\mu_J > 22$ mag arcsec^{-2}) in the $R < R_{500}$ region of $z = 1$ clusters grows by 2–4 times by the present day, whereas DeMaio et al. (2020) showed that the amount of stellar mass within the central 100 kpc of clusters continued growing until $z \sim 0.4$. These works suggest the intracluster light beyond 100 kpc will likely continue growing to the present day, and the mass growth rate of intracluster stars exceeds that of the halo. Therefore, the diffuse light we see in the proto-clusters is likely to grow both in size and mass over the following 10 Gyr.

5.3 Prospects for detecting proto-cluster intracluster light with ESA's Euclid Mission

Our discovery of intracluster light at $z \sim 2$ means that it is possible to use the signature of diffuse low surface brightness light and low stellar mass concentrations to identify clusters and proto-clusters from high-resolution images, which will be provided by ESA's *Euclid* mission. This is particularly useful at $z > 1.5$, where the photometric redshifts that *Euclid*'s cluster finders use are not precise enough to identify galaxy clusters. The presence, or lack, of intracluster light can be used to remove contaminants from the cluster catalogues based on photometric redshifts. Furthermore, since the presence of diffuse light is unique to the central galaxies in proto-clusters, this is an excellent way to identify the dominant halo within a proto-cluster.

The *Euclid* Wide Survey is predicted to reach a surface brightness of 29.1 mag arcsec^{-2} in VIS (3σ over 100 arcsec^2) and 27.7 mag arcsec^{-2} for Y, J, and H−band NISP images (Borlaff et al. 2022; Scaramella et al. 2022), while the Deep Survey will reach 2 mag fainter. This means that the Deep Survey will reach similar depths to the *HST* $F140W$ images we use in this work (29.2 and 30.3 mag/arcsec^2 in CARLA J1018 and XLSSC-122, respectively) but over a much larger area.

It is also likely that intracluster light will be detected in the Wide Survey of *Euclid*. The surface brightness of the intracluster light in the region between 10 and 50 kpc (∼100 arcsec^2) in both proto-clusters presented in this work is $[F140W] \sim 26.5$ mag arcsec^{-2}, and $[F140W] \sim 27.1$ mag arcsec^{-2} averaged over the larger region between 10 and 100 kpc (∼ 430 arcsec^2). Thus, we predict that the intracluster light in both proto-clusters should be detected in the near-infrared images of *Euclid*'s Wide Survey.

Whether the intracluster light is also detected in the VIS images depends on the colour of the light. The reddest colour of the intracluster light that we measure is $[z] - [F140W] \sim 2$, which means the surface brightness could be as low as $z = 29.1$ mag arcsec^{-2}. The VIS instrument covers the wavelength range 550–900 nm, so it covers light blueward of the z−band image we use in this work. Hence, intracluster light at $z \sim 2$ is likely to be detected in VIS images of the Deep Survey, but we are unlikely to detect intracluster light in the Wide Survey unless the intracluster stars are young and blue. We conclude that the NISP images are better suited to search for intracluster light in distance clusters and proto-clusters.

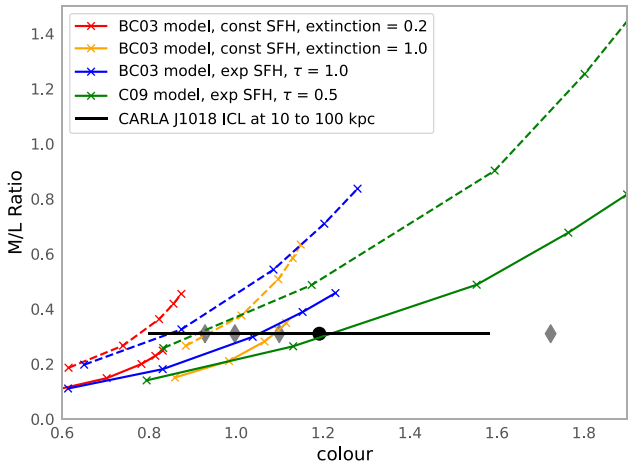

Figure 9. The relationship between the $[z - F140]$ colour and mass-to-light ratio for galaxies at $z = 1.96$. The colour of the intracluster light in CARLA J1018 between 10 and 100 kpc is shown as the black point with 1σ uncertainties. The grey diamonds display the variety of intracluster light colour in the four rectangular regions described in the text. The coloured lines show the mass-to-light ratio from galaxies simulated with different star formation histories and Chabrier (solid) or Salpeter (dashed) initial mass functions. The crosses from the bottom left to top right of each line mark the colour of galaxies formed at $z = 2.5$, 3, 4, 5, and 6 and observed at $z = 1.96$. The lowest possible colour of the intracluster corresponds to a minimum mass-to-light ratio of 0.14. We take this to be the minimum possible mass-to-light ratio for the intracluster light in CARLA J1018.

Additionally, the intracluster light maps in Fig. 3 show that the light is not uniform and brighter regions of diffuse emission will appear well above *Euclid*'s detection limits. This will allow detailed measurements of the morphology and colours of the intracluster light.

The Vera C. Rubin Observatory (LSST) will provide complementary data in the optical bands to even greater depth than the *Euclid* survey. However, the prospects of detecting intracluster light in proto-clusters with LSST are limited for two reasons. First, the survey is optimized for depth in the optical bands and the z and y band images will be the shallowest. Therefore, the LSST survey will probe the rest-frame ultraviolet light from proto-cluster intracluster stars, which will only be prominent when the intracluster stars are young. Secondly, the relatively poor spatial resolution of LSST data compared to *Euclid* means that it will be harder to separate galactic light from diffuse intracluster light in the dense core of proto-clusters.

5.4 The impact of the mass-to-light ratio on the stellar mass concentration

The uncertainties on the colour, and hence mass-to-light ratio, of the intracluster light beyond 10 kpc within CARLA J1018, and beyond 50 kpc in XLSSC 122 can significantly affect our conclusions of a low stellar mass concentration, so it is worth investigating how different mass-to-light ratios will affect our conclusions. First, we consider an extreme case in which the mass-to-light ratio beyond 50 kpc of XLSSC 122 is extremely low such that the mass in this region is negligible. Even in this extreme case, the mass concentration would increase to only 0.46 ± 0.04, which is still compatible with the trend for other clusters seen in Fig. 6 and lies far below the model predictions of Contini & Gu (2021).

Next, we consider the lowest plausible value of the mass-to-light ratio for the ICL beyond 10 kpc in CARLA J1018. We start by examining colour variations in the ICL. We place four rectangular apertures across the brightest region of the ICL in the $F140W$ image but not covering the central 10 kpc from the BCG. The centres of the apertures were at [154.6255, 5.5183], [154.6264, 5.5175], [154.6279, 5.5161], and [154.6288, 5.5152], each of 39×93 kpc and at an 45° angle. All apertures had measurable $F140W$ and $z-$band fluxes at more than a 1.5σ level. The colours of the four regions were $[z] - [F140W] = 0.9$, 1.1, 1.0, and 1.6 from south-east to north-west, which means there is colour variation in the intracluster light and a single mass-to-light ratio does not capture the complexity of this system. None the less, we can use a single mass-to-light ratio to estimate a minimum mass in this outer region and take that as a lower limit to the true mass. The colour of the intracluster light in the annulus of 10–100 kpc is $[z] - [F140W] = 1.2 \pm 0.4$. Thus, the minimum colour of the intracluster light, assuming maximal measurement uncertainties, is $[z] - [F140W] = 0.8$. The intracluster light in all smaller regions have a redder colour, reassuring us that this is the bluest possible colour of the intracluster light.

We compare this colour to a set of stellar population models in Fig. 9. Such a blue colour can only be achieved with a stellar population model that is actively forming new stars, such as a constant star formation history or a very young (0.5 Gyr), exponentially declining model with a long time-scale for the decay of the star formation rate. The mass-to-light ratio also depends on the assumed IMF, with a Salpeter IMF producing a higher mass-to-light ratio than the Chabrier IMF. Throughout this work, we assume a Chabrier IMF; however, evidence points to a peculiar stellar IMF in clusters (Friedmann & Maoz 2018). By assuming a Chabrier IMF, we therefore take the minimum plausible mass-to-light ratio for the intracluster light. For a Chabrier IMF, a colour of $[z] - [F140W] = 0.8$ corresponds to a minimum mass-to-light ratio of 0.14. Applying this minimum mass-to-light ratio to the intracluster light beyond 10 kpc, the luminosity concentration of 0.23 implies a mass concentration of 0.66. This value is still compatible with the observed trend for lower-redshift cluster BCGs and below the measurements for other massive galaxies in the proto-cluster.

5.5 Defining the BCGs in the proto-clusters

The selection of the BCG can also affect our conclusions of a low stellar mass concentration. There is no other plausible candidate for the BCG in XLSSC 122 since the galaxy we have labelled as the BCG is 1 mag brighter and 7.6 times more massive than the second ranked galaxy in this proto-cluster (Noordeh et al. 2021). On the other hand, the selection of galaxy *a* as the BCG of CARLA J1018 is not certain as galaxies *b*, *c*, and *d*, as well as the quasar, could all be the most massive galaxy in the proto-cluster. Galaxy *b* is also brighter than galaxy *a* in F140W, although both galaxies have consistent fluxes within uncertainties in the $K-$band, and as can be seen from Fig. 2, the SED fits predict that redward of 2 microns, and galaxy *a* is likely to be brighter than galaxy *b*. We therefore used the local surface density of galaxies to determine which of these galaxies is most likely to be at the barycentre of the proto-cluster. We selected galaxy *a* because it is the most massive and has the highest galaxy density on the scale of 100 kpc out of all galaxies in the proto-cluster.

Whilst these reasons justify our choice of galaxy *a* as the BCG, we also find that our results do not qualitatively change if we chose galaxies *b*, *c*, or *d* to be the BCG: we still find significant diffuse light beyond 10 kpc of the BCG core regardless of which galaxy is chosen to be the BCG. Quantitatively, the amount of light within the 100 kpc radius would be reduced if the BCG was chosen to lie at the edge of the high-density region shown in the insert of

Fig. 1, and the amount of diffuse light that would be classified as residing beyond 100 kpc would increase. For example, if we selected galaxy *b* as the BCG, then we obtain a BCG + ICL observed F140W magnitude of 21.70 ± 0.02 mag within 10 kpc and 20.9 ± 0.2 mag in the 10–100 kpc annulus. This results in a light concentration of 0.32 ± 0.03. This is slightly more concentrated than if we selected galaxy *a* as the BCG, but it is still far lower than the light concentration found for the other massive proto-cluster galaxies located outside the core. Therefore, the exact values of the mass and light concentrations will increase, although they are still low compared to other massive galaxies, both within and beyond the proto-cluster. Thus, our conclusion remains valid as long as the dense region in the insert of Fig. 1 is the barycentre of the proto-cluster.

The argument given above only holds if we can use the surface density of galaxies as a proxy for the true 3D density; if the dense core region in the insert of Fig. 1 is only due to the projection of unrelated galaxies, then this region may not be the barycentre of the proto-cluster. We therefore compare the probability that the galaxy overdensity is due to a chance line-of-sight distribution to the probability that these galaxies are in close proximity and are interacting with each other.

The area of the region depicted in the insert of Fig. 1 is 0.31 × 0.32 co-moving Mpc^2 (16.8 × 17.1 arcsec^2) and the line-of-sight co-moving radial distance spanned by the interval $\Delta z = 0.04$ is 60.4 Mpc, so the volume is 6.1 Mpc^3. The number density of $>10^{11}$ M$_\odot$ galaxies at $z \sim 2$ is 10^{-4} Mpc^{-3} (Muzzin et al. 2013) so the probability of observing any galaxy more massive than 10^{11} M$_\odot$ in this volume is 0.06 per cent. The probability of detecting five unrelated galaxies, of more than 10^{11} M$_\odot$, within this volume is vanishingly small at less than one in a trillion.

On the other hand, the chance of observing two massive galaxies that are in the process of merging is much higher. Simulations predict that a 10^{11} M$_\odot$ galaxy at $z = 2$ will merge with another galaxy, of at least a quarter of its mass, at a rate of 0.15 Gyr^{-1} (Rodriguez-Gomez et al. 2015). Galaxy mergers can be identified as close pairs of galaxies, and the length of time a merger is visible depends on the projected separation and mass ratio of the pair. For galaxies within a 1: 4 mass ratio, this time-scale varies from a few hundred Myr to 1.5 Gyr depending on the projected separation (Lotz et al. 2011). The projected separations of the galaxies in the core region range between 12 and 36 kpc (proper) so these mergers will be visible for an average of 0.6–1 Gyr. Thus, the probability of observing a massive galaxy undergoing a merger with another nearby galaxy is 10–15 per cent. Since there are five galaxies more massive than 10^{11} M$_\odot$ in the core, and hence 10 unique pairs, there is a 60–80 per cent chance that we would observe these galaxies undergoing a merger. Assuming each merger is mutually exclusive and treating the closer merger pair as a single entity, the probability of observing five massive galaxies merging at the same time is 0.01–0.05 per cent. This is much higher than the chance of observing five unrelated massive galaxies distributed across the 60.4 cMpc line of sight; hence it is more likely that the dense galaxy group we have observed in CARLA J1018 is the barycentre of the proto-cluster than a chance line of sight alignment.

The space density of $>10^{11}$ M$_\odot$ galaxies is 10^{-4} Mpc^{-3} (Muzzin et al. 2013), and we have calculated that between one in a 100 to one in 20 of these will be undergoing extreme merging events such as that seen in the core of the CARLA J1018 proto-cluster. This means the space density of such extreme merging events is 10^{-8} Mpc^{-3}. This is the same space density as galaxy clusters with masses greater than 10^{15} M$_\odot$ in the nearby Universe (Vikhlinin et al. 2009). It is therefore plausible that such extreme merging events signpost the formation of the core within the most massive galaxy clusters.

6 CONCLUSIONS

We report on the detection of intracluster light within two proto-clusters at $z \sim 2$ using deep *HST* near-infrared images. This extends our understanding of intracluster light to the numerous group-sized haloes that exist at this redshift; previous measurements focused on the most extreme (and rare) cluster-sized haloes at $z \sim 1.5$, which may not be typical cluster progenitors.

We identified the BCGs of the proto-clusters as the most massive galaxies within the densest regions of the proto-clusters, and measure the amount of diffuse light surrounding these galaxies. We found that the flux of diffuse light between 10 and 100 kpc is more than double the flux from within 10 kpc. We showed that this extended morphology is similar to the profiles of BCGs within massive clusters at $1.24 < z < 1.75$ that are known to host intracluster light. Furthermore, this profile differs from the other massive galaxies in the proto-cluster, whose light profiles are at least a factor of 3 more concentrated than the BCGs. Based on these observations, we conclude that the proto-clusters contain significant intracluster light.

We used the colour of the intracluster light to estimate its mass-to-light ratio and calculate the concentration of stellar mass in the core of the proto-clusters. We found that only a quarter to a half of the stellar mass within 100 kpc is located within the central 10 kpc. We combine our data with that of DeMaio et al. (2020) to show that this low concentration is comparable to that found in similar-sized haloes at lower redshifts, and such low concentrations at $z \sim 2$ are in disagreement with the semi-analytic models of intracluster light by Contini & Gu (2021). Our discovery implies that the formation of the intracluster light began earlier than the $z \sim 1$–1.5 period predicted by these models.

To investigate how this intracluster light could form so early, we compared the stellar mass concentrations in clusters and proto-clusters to that of central galaxies of massive haloes in the Hydrangea hydrodynamical simulations (Bahé et al. 2017). We found that these simulations agree with the trend in the observations: the stellar mass concentration depends on the halo mass but does not depend on redshift. Hydrangea also predicts that intra-halo stars are ubiquitous in massive haloes at all redshifts, and even found in haloes with masses as low as 10^{12} M$_\odot$. We interpret these findings as evidence that pre-processed free-floating stars from accreted haloes is a major contributor to the intracluster light within 100 kpc of clusters and protoclusters, while few of the stars in this region were stripped from orbiting satellite galaxies.

ACKNOWLEDGEMENTS

We thank the reviewer for useful comments and Leonardo Ferreira for helping with the technical details of *HST* data reduction. SW thanks the University of Nottingham, UK, Vice Chancellor International Scholarship. NAH thanks the Science and Technology Facilities Council, UK, consolidated grant ST/T000171/1. GN thanks the Natural Sciences and Engineering Research Council Canada, Discovery Grant and Discovery Accelerator Supplement and the Canadian Space Agency, grant 18JWST-GTO1. YMB thanks the Dutch Science Organisation (NWO), Veni grant 639.041.751. JM

thanks the George P. and Cynthia Woods Mitchell Institute for Fundamental Physics and Astronomy at Texas A&M University. DW thanks the German Research Foundation, Emmy Noether Grant WY 179/1-1, the Daimler and Benz Foundation and the German Space Agency, Verbundforschung grant 50 OR 2213. Based on observations collected at the European Organisation for Astronomical Research in the Southern Hemisphere under ESO programmes 094.A-0343(C), 094.A-0343(D), 094.A-0343(E), 096.A-0317(A), 096.A-0317(B), and 096.A-0317(C).

DATA AVAILABILITY

All data used in the analysis of this paper can be downloaded from the Mikulski Archive for Space Telescopes, https://archive.stsci.edu, or the ESO Science Archive Facility, http://archive.eso.org.

REFERENCES

Aghanim N. et al., 2020, A&A, 641, A6
Alonso Asensio I., Dalla Vecchia C., Bahé Y. M., Barnes D. J., Kay S. T., 2020, MNRAS, 494, 1859
Bahé Y. M. et al., 2017, MNRAS, 470, 4186
Bahé Y. M. et al., 2019, MNRAS, 485, 2287
Bertin E., Arnouts S., 1996, A&AS, 117, 393
Borlaff A. S. et al., 2022, A&A, 657, A92
Brammer G., 2019, Astrophysics Source Code Library, record ascl 1905.001
Brammer G. B., van Dokkum P. G., Coppi P., 2008, ApJ, 686, 1503
Bruzual G., Charlot S., 2003, MNRAS, 344, 1000
Burke C., Collins C. A., Stott J. P., Hilton M., 2012, MNRAS, 425, 2058
Burke C., Hilton M., Collins C., 2015, MNRAS, 449, 2353
Chabrier G., 2003, PASP, 115, 763
Conroy C., Gunn J. E., White M., 2009, ApJ, 699, 486
Contini E., De Lucia G., Villalobos C., Borgani S., 2013, MNRAS, 437, 3787
Chu A., Durret F., Márquez I., 2021, A&A, 649, A42
Collins C. A. et al., 2009, Nature, 458, 603
Conroy C., Gunn J. E., 2010, ApJ, 712, 833
Contini E., 2021, Galaxies, 9, 60
Contini E., Gu Q., 2020, ApJ, 901, 128
Contini E., Gu Q., 2021, ApJ, 915, 106
Cooke E. A. et al., 2015, MNRAS, 452, 2318
De Lucia G., Blaizot J., 2007, MNRAS, 375, 2
DeMaio T. et al., 2019, MNRAS, 491, 3751
DeMaio T. et al., 2020, MNRAS, 491, 3751
Friedmann M., Maoz D., 2018, MNRAS, 479, 3563
Golden-Marx J. B. et al., 2022, ApJ, 928, 28
Hatch N. A., Overzier R. A., Röttgering H. J. A., Kurk J. D., Miley G. K., 2008, MNRAS, 383, 931
Ivanov V. D., Rieke M. J., Engelbracht C. W., Alonso-Herrero A., Rieke G. H., Luhman K. L., 2004, ApJS, 151, 387
Joo H., Jee M. J., 2023, Nature, 613, 37
Ko J., Jee M. J., 2018, ApJ, 862, 95
Kriek M., van Dokkum P. G., Labbé I., Franx M., Illingworth G. D., Marchesini D., Quadri R. F., 2009, ApJ, 700, 221
Lotz J. M., Jonsson P., Cox T. J., Croton D., Primack J. R., Somerville R. S., Stewart K., 2011, ApJ, 742, 103
Mantz A. B. et al., 2018, A&A, 620, A2
Mei S. et al., 2023, A&A 670 58
Merritt D., 1984, ApJ, 276, 26
Montes M., 2022, Nature Astron., 6, 308
Montes M., Trujillo I., 2018, MNRAS, 482, 2838
Muldrew S. I., Hatch N. A., Cooke E. A., 2015, MNRAS, 452, 2528
Muzzin A. et al., 2013, ApJ, 777, 18
Navarro J. F., Frenk C. S., White S. D. M., 1997, ApJ, 490, 493
Noirot G. et al., 2016, ApJ, 830, 90
Noirot G. et al., 2018, ApJ, 859, 38
Noordeh E., Canning R. E. A., Willis J. P., Allen S. W., Mantz A., Stanford S. A., Brammer G., 2021, MNRAS, 507, 5272
Pickles A. J., 1998, PASP, 110, 863
Rodriguez-Gomez V. et al., 2015, MNRAS, 449, 49
Rudick C. S., Mihos J. C., McBride C., 2006, ApJ, 648, 936
Scaramella R. et al., 2022, A&A, 662, A112
Schaye J. et al., 2015, MNRAS, 446, 521
Schirmer M., 2013, ApJS, 209, 21
Schlegel D. J., Finkbeiner D. P., Davis M., 1998, ApJ, 500, 525
Skrutskie M. F. et al., 2006, AJ, 131, 1163
Vandame B., 2004, PhD thesis, Université de Nice-Sophia Antipolis, France
Vikhlinin A. et al., 2009, ApJ, 692, 1060
Whiley I. M. et al., 2008, MNRAS, 387, 1253
Willis J. P. et al., 2013, MNRAS, 430, 134
Willis J. P. et al., 2020, Nature, 577, 39
Wylezalek D. et al., 2013, ApJ, 769, 79
Wylezalek D. et al., 2014, ApJ, 786, 17
Zhang Y. et al., 2019, ApJ, 874, 165

This paper has been typeset from a TEX/LATEX file prepared by the author.